SUPPORTING INFORMATION

Hierarchical porous Fe_3C@Fe-N-C catalysts from tannin-Fe(III) complexes for efficient oxygen reduction

Sara Pérez-Rodríguez[*,1,2], Daniel Torres[1,2], María Teresa Izquierdo[2], Andrea Zitolo[3], Nicolas Bibent[4], Moulay Sougrati[4], Frédéric Jaouen[4], Alain Celzard[1,5], Vanessa Fierro[*,1]

[1] Université de Lorraine, CNRS, IJL, F-88000 Epinal, France

[2] Instituto de Carboquímica (ICB-CSIC), Miguel Luesma Castan 4, Zaragoza, E-50018, Spain

[3] Synchrotron SOLEIL, L'Orme des Merisiers, Départementale 128, 91190, France

[4] ICGM, Univ. Montpellier, CNRS, ENSCM, Montpellier, France

[5] Institut Universitaire de France (IUF), F-75231 Paris, France

*Corresponding authors: sperez@icb.csic.es, Vanessa.Fierro@univ-lorraine.fr

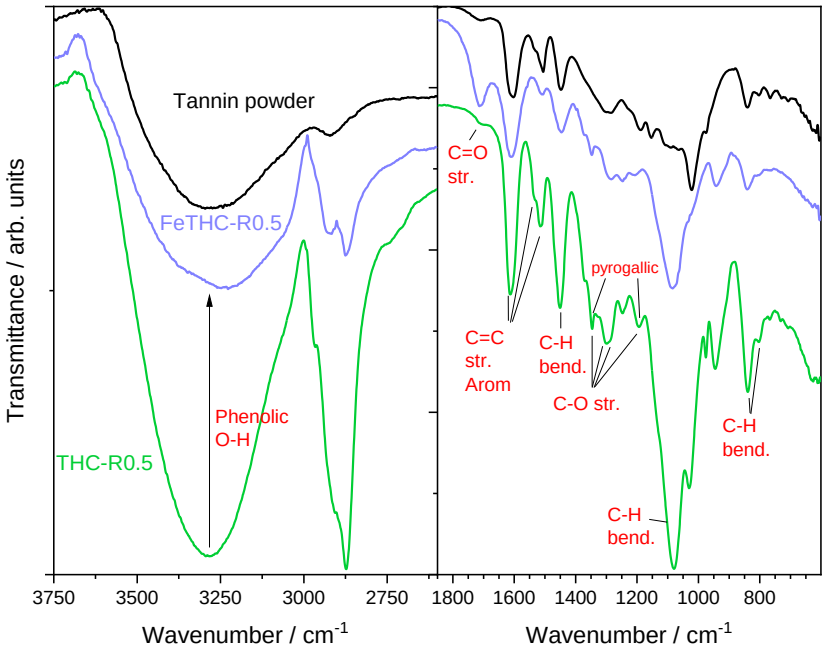

Figure S1. FTIR spectra of dried mimosa tannin and hydrochars obtained with and without addition of iron (III) chloride, using a Pluronic-127/mimosa tannin mass ratio of 0.5 (FeTHC-R0.5 and THC-R0.5, respectively).

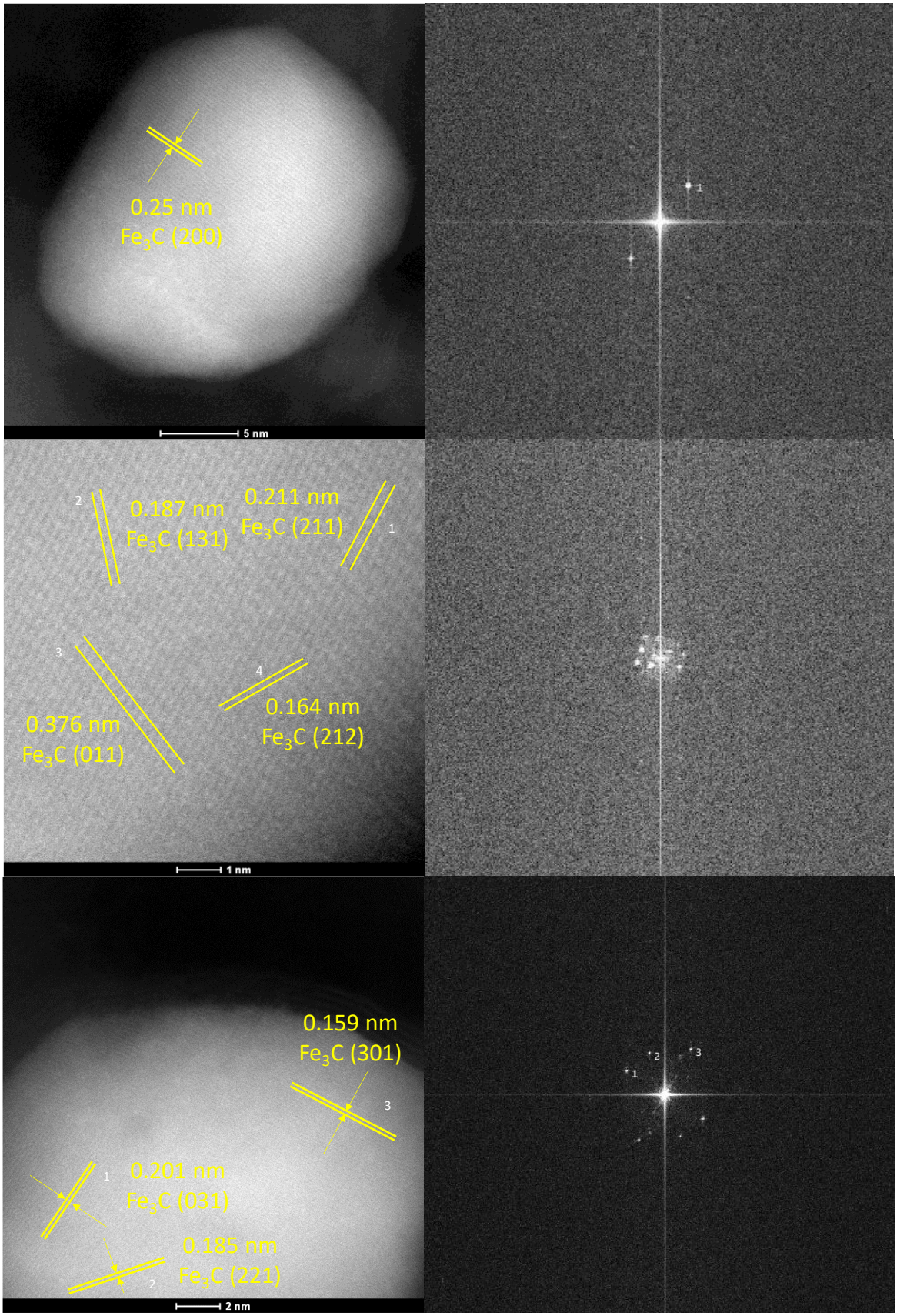

Figure S2. Fe_3C lattice fringes for Fe-N-(FeTC-R0.5). Aberration-corrected HAADF-STEM images and FFT patterns of different Fe_3C particles. The images were recorded using an analytical Titan microscope.

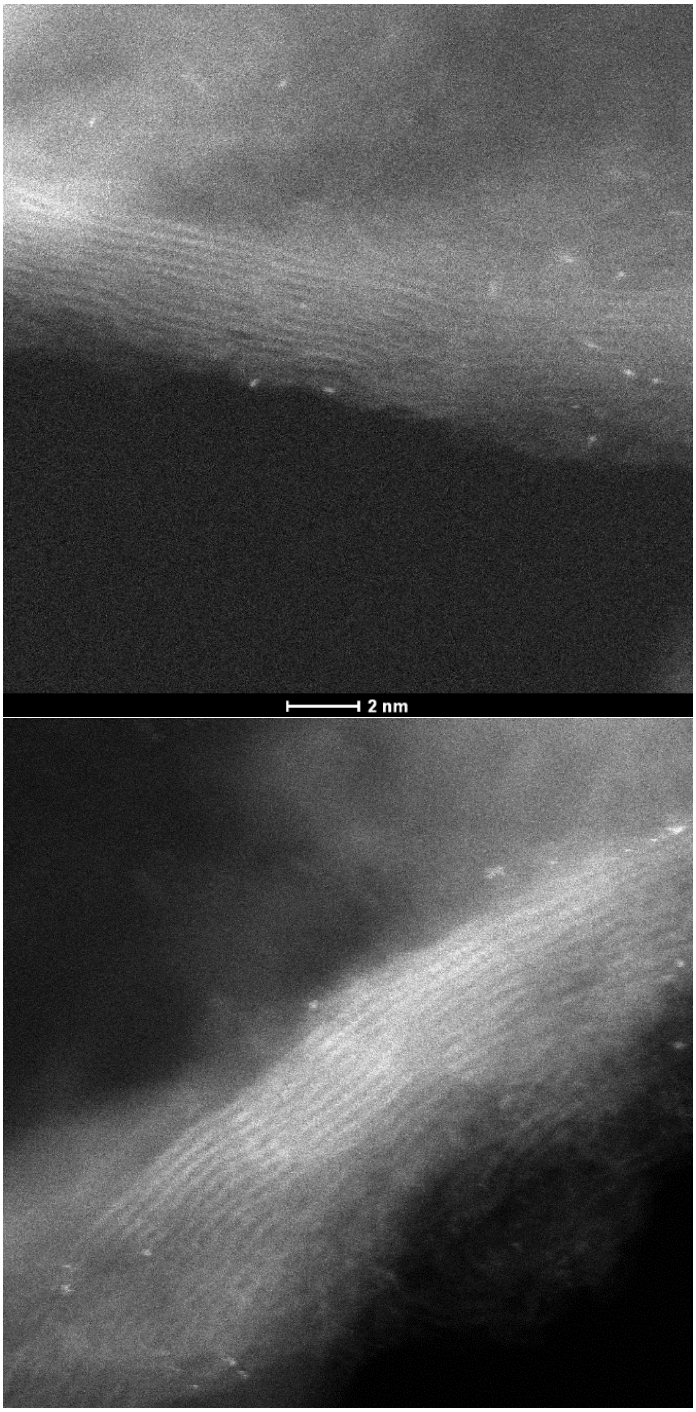

Figure S3. Aberration-corrected HAADF-STEM images for Fe-N-(FeTC-R0.5). The images were recorded using an analytical Titan microscope.

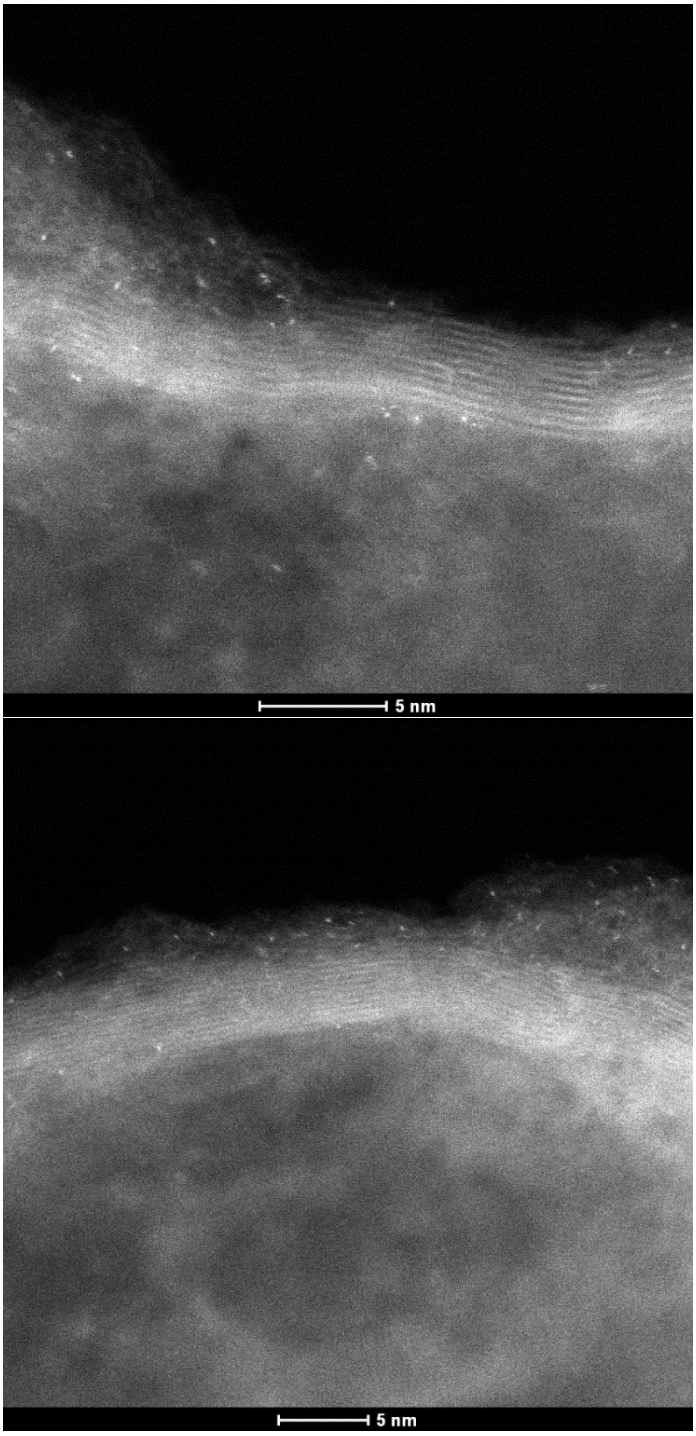

Figure S3. *(continued)*

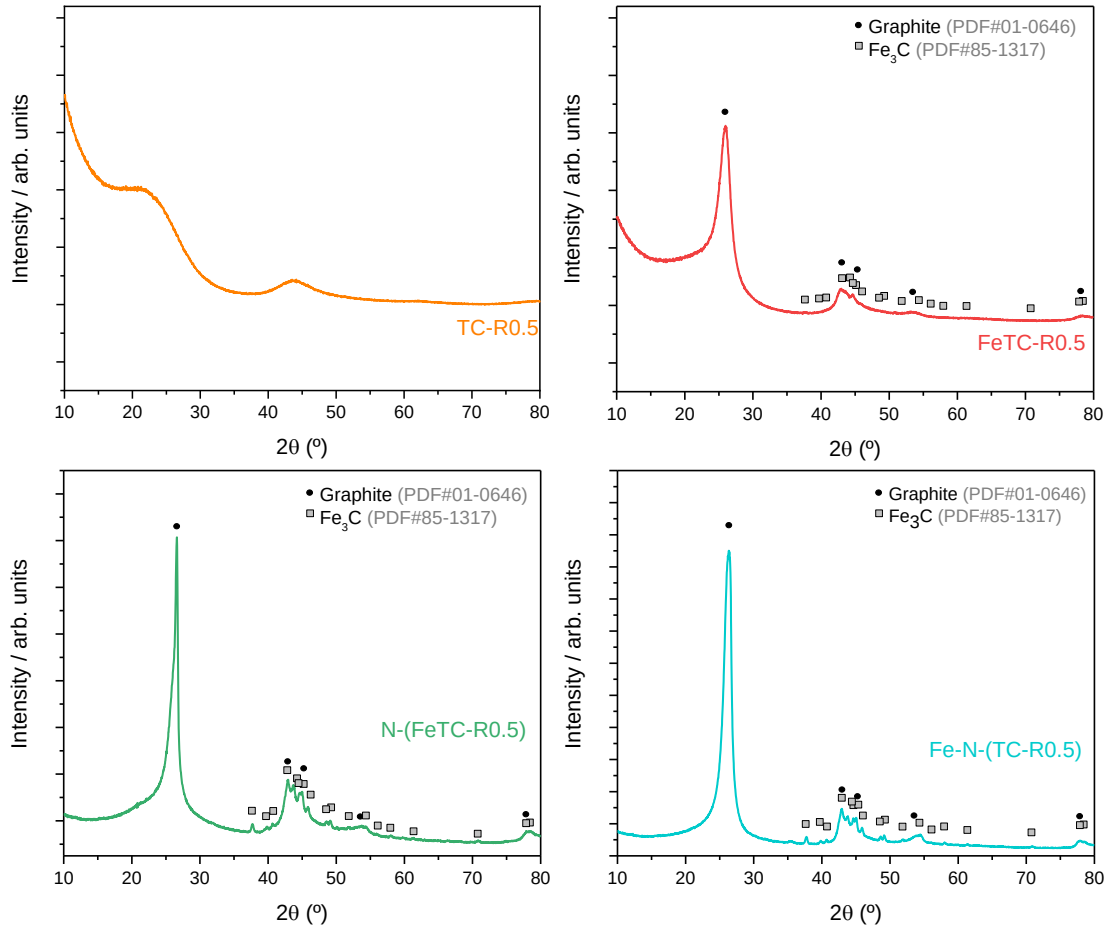

Figure S4. XRD patterns of TC-R0.5, FeTC-R0.5, Fe-N-(TC-R0.5) and N-(FeTC-R0.5).

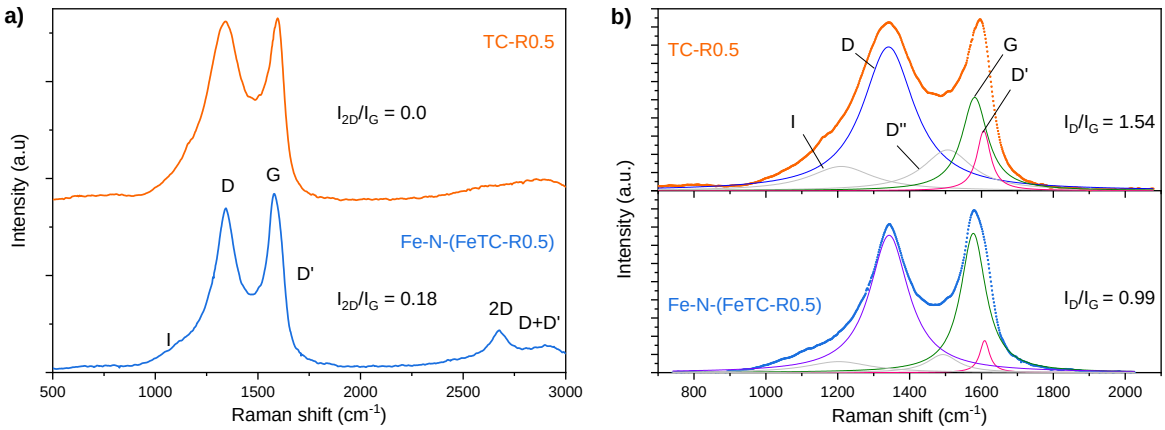

Figure S5. (a) Raw first- and second-order Raman spectra for TC-R0.5 and Fe-N-(FeTC-R0.5). (b) Deconvolution of first-order Raman profiles into 5 bands. Intensity ratios of deconvoluted bands D (~1343 cm^{-1}) and 2D (~2676 cm^{-1}) to G (~1580 cm^{-1}) are included in the figures.

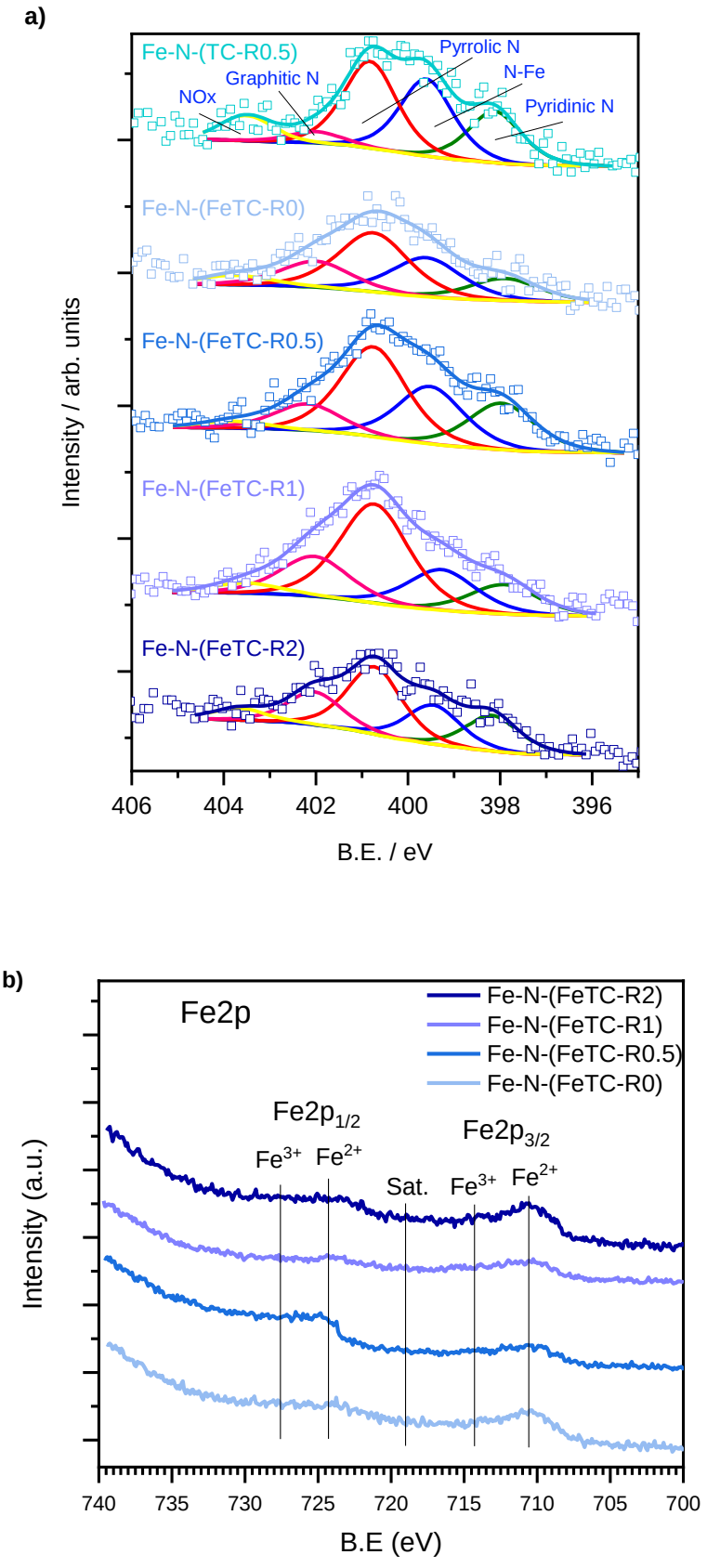

Figure S6. (a) Deconvolution of high-resolution N1s XPS spectra and, (b) high-resolution Fe2p XPS spectra of tannin-derived electrocatalysts.

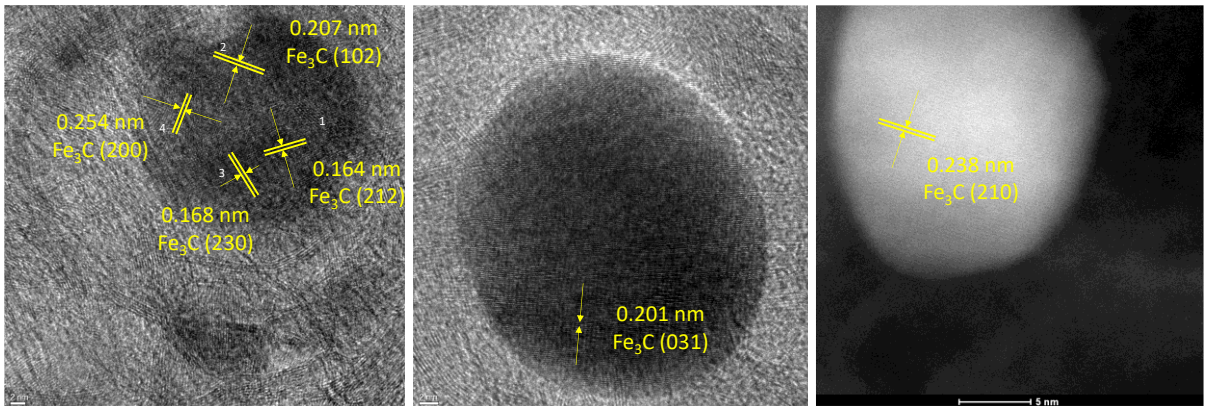

Figure S7. Fe_3C lattice fringes for FeTC-R0.5. Aberration-corrected HRTEM and HAADF-STEM images of different Fe_3C particles obtained using an analytical Titan microscope.

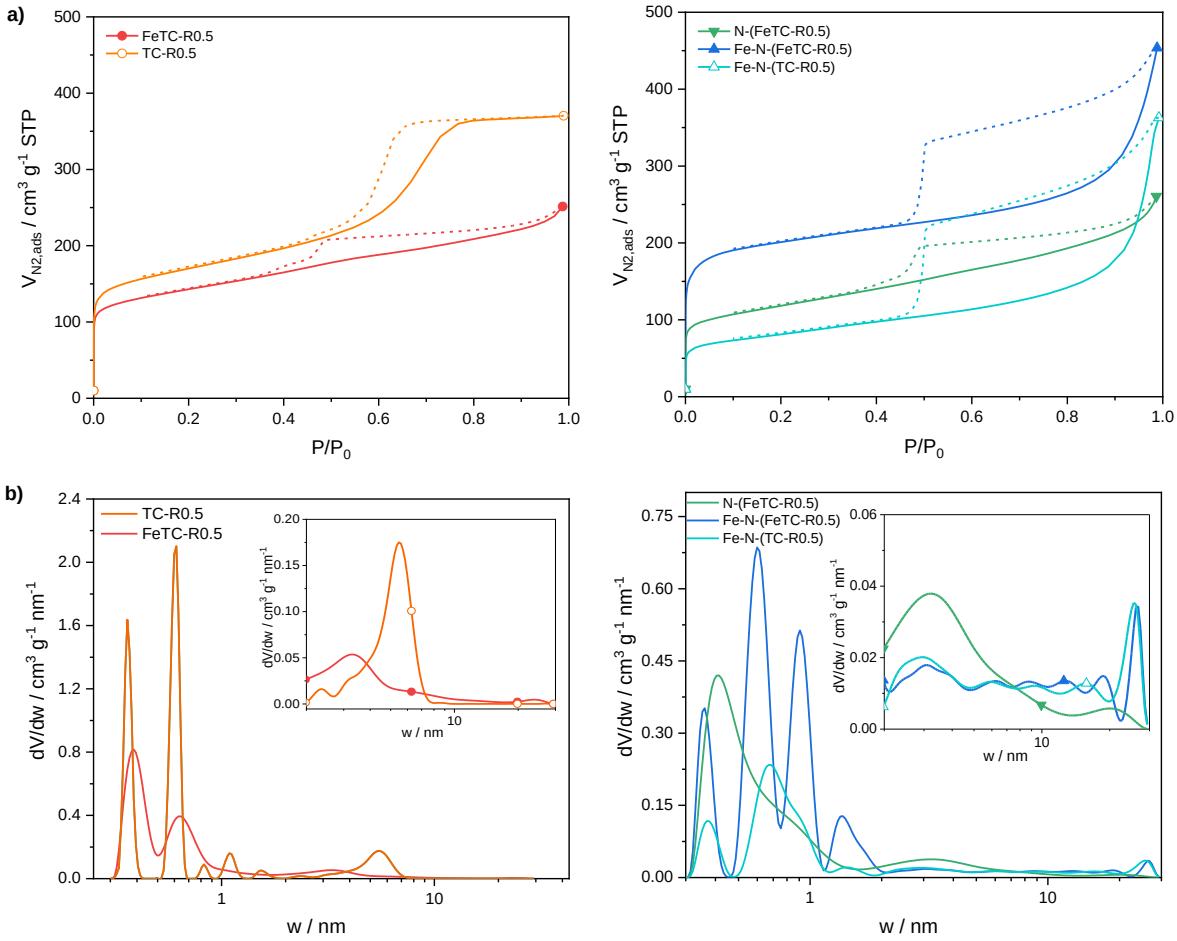

Figure S8. Textural properties of Fe-N-(FeTC-R0.5) and reference materials: (a) N_2 adsorption (solid curves) and desorption (dotted curves) isotherms at -196 °C; (b) Pore size distribution (PSD) determined by applying the NLDFT method to N_2 and H_2 isotherms. The insets show zooms.

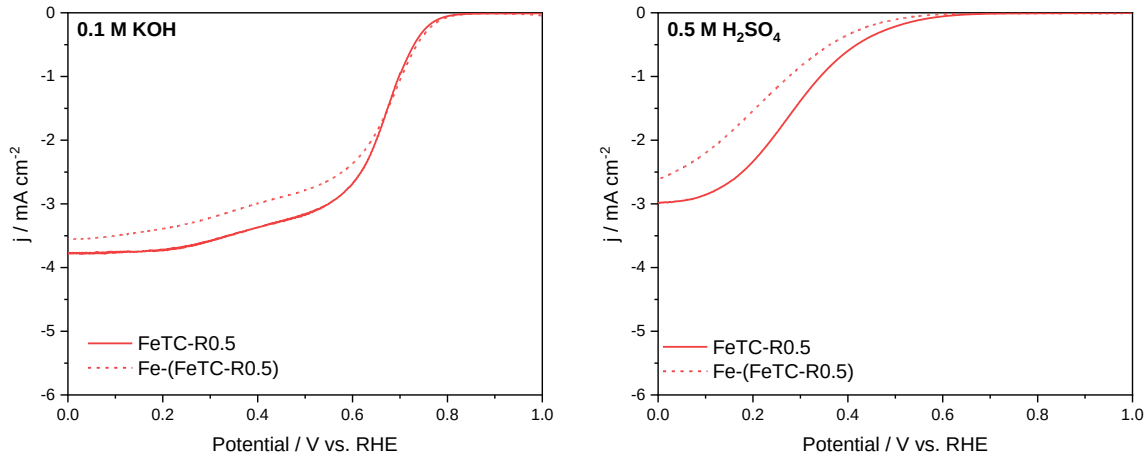

Figure S9. LSV curves of FeTC-R0.5 and Fe-(FeTC-R0.5) in O_2-saturated aqueous solutions of 0.1 M KOH (left) and 0.5 M H_2SO_4 (right) at 5 mV s^{-1} and 1600 rpm.

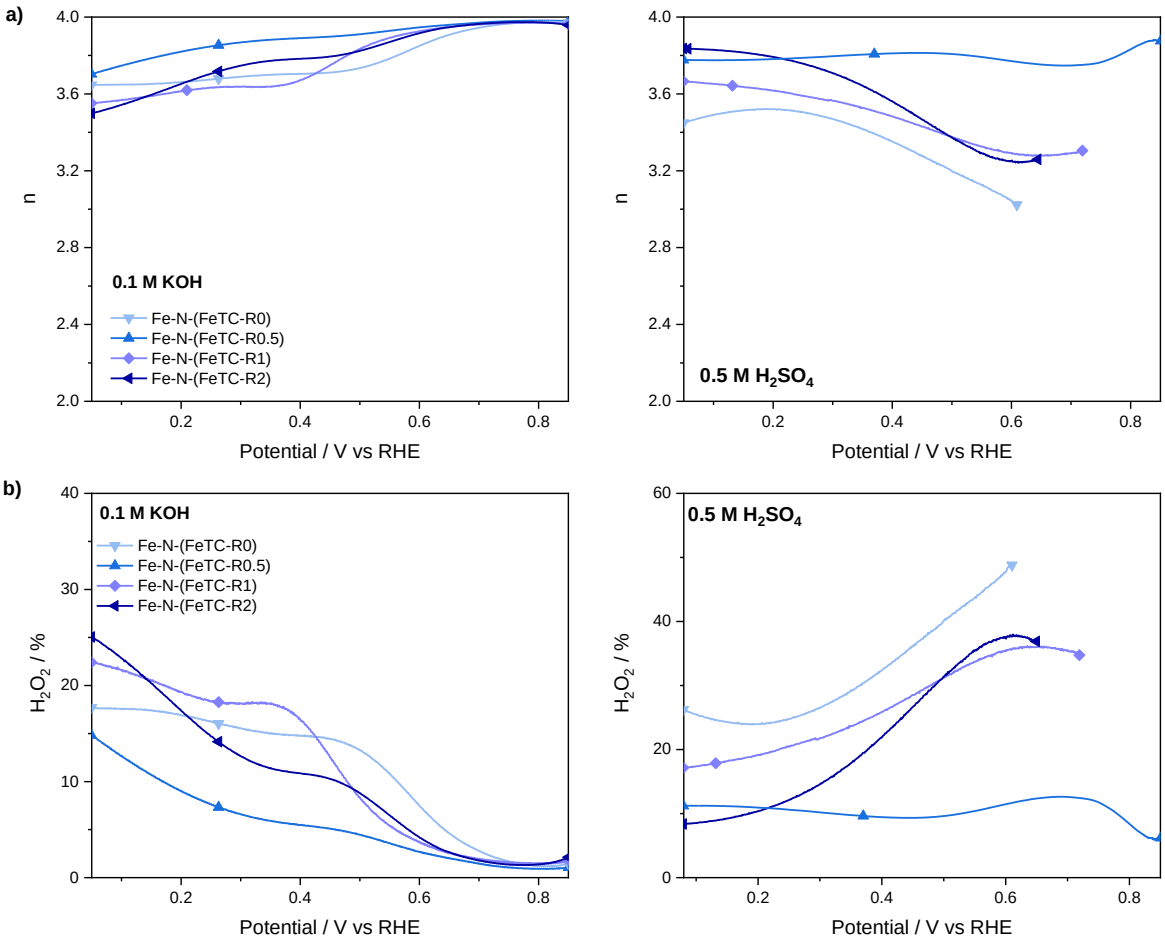

Figure S10. (a) Electron transfer number, and (b) peroxide yields as a function of applied potential for tannin-derived catalysts obtained using different Pluronic-127/mimosa tannin mass ratios (*R*) in O_2-saturated aqueous solutions of 0.1 M KOH (left) and 0.5 M H_2SO_4 (right) at 5 mV s^{-1} and 1600 rpm.

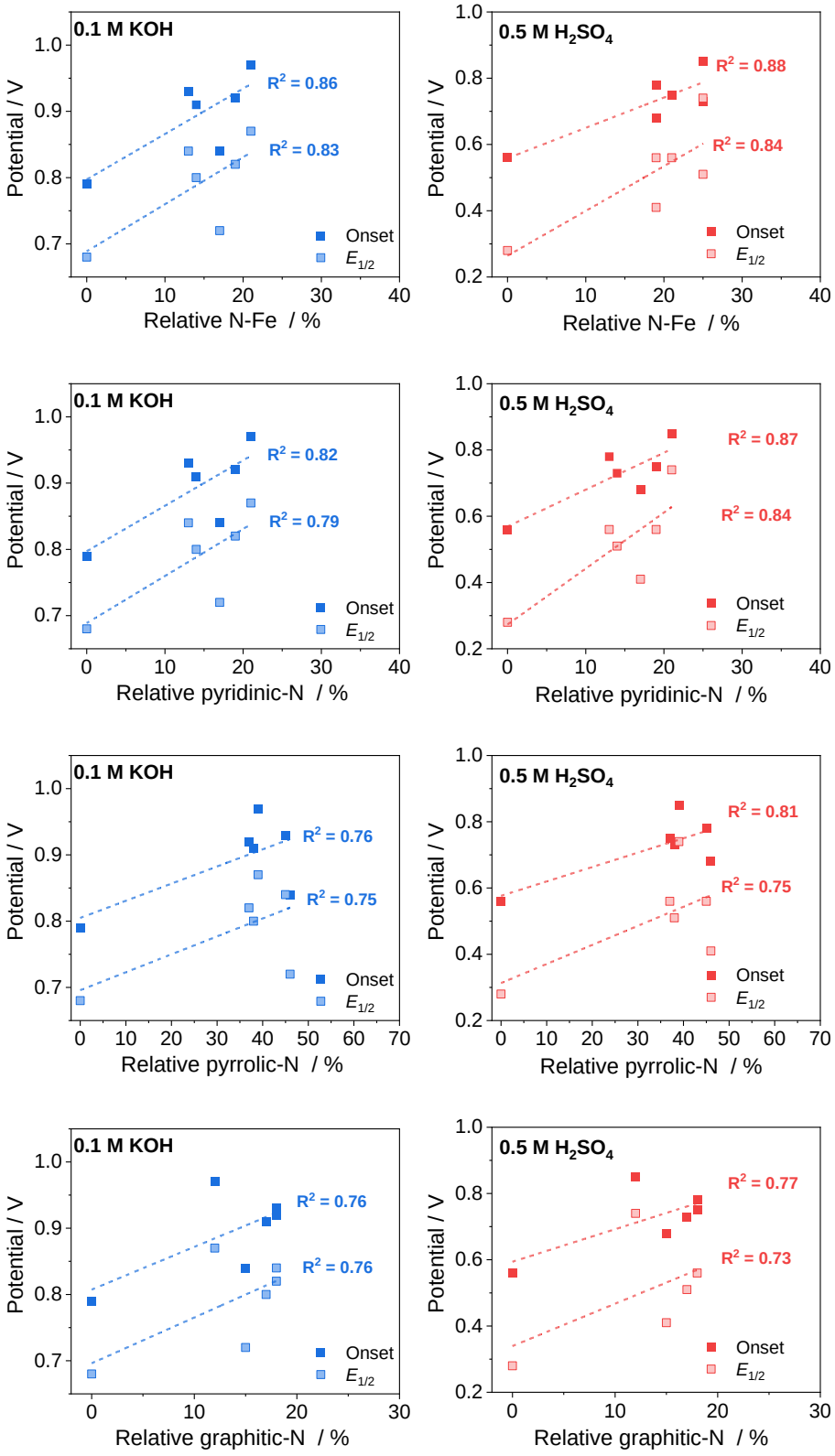

Figure S11. Onset potential and $E_{1/2}$ as a function of the relative contribution of surface N moieties determined by XPS in alkaline (left), and acidic (right) electrolytes, for electrocatalysts obtained from Fe-containing, tannin-derived hydrochars.

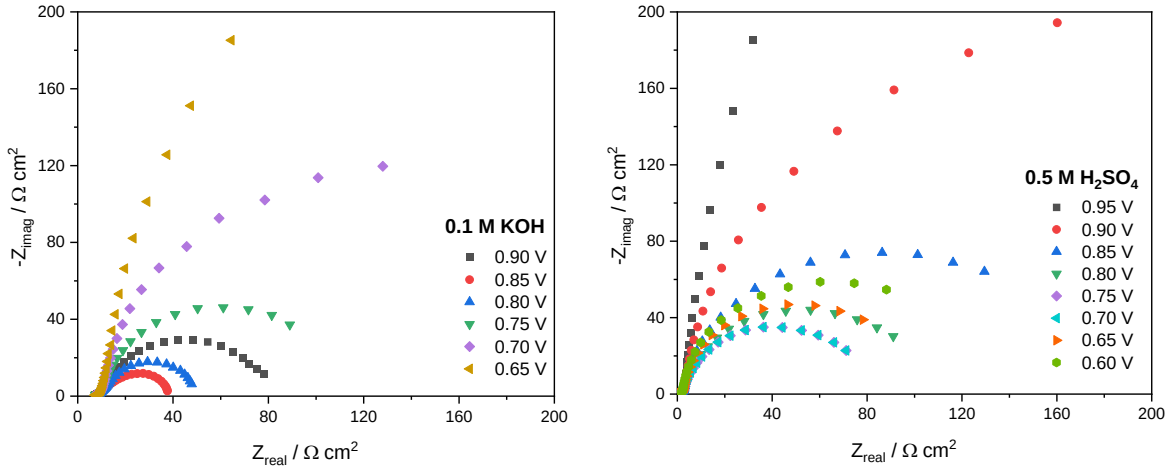

Figure S12. Nyquist plots for Fe-N-(FeTC-R0.5) in 0.1 M KOH (left) and 0.5 M H_2SO_4 (right) aqueous solutions saturated with oxygen at 1600 rpm.

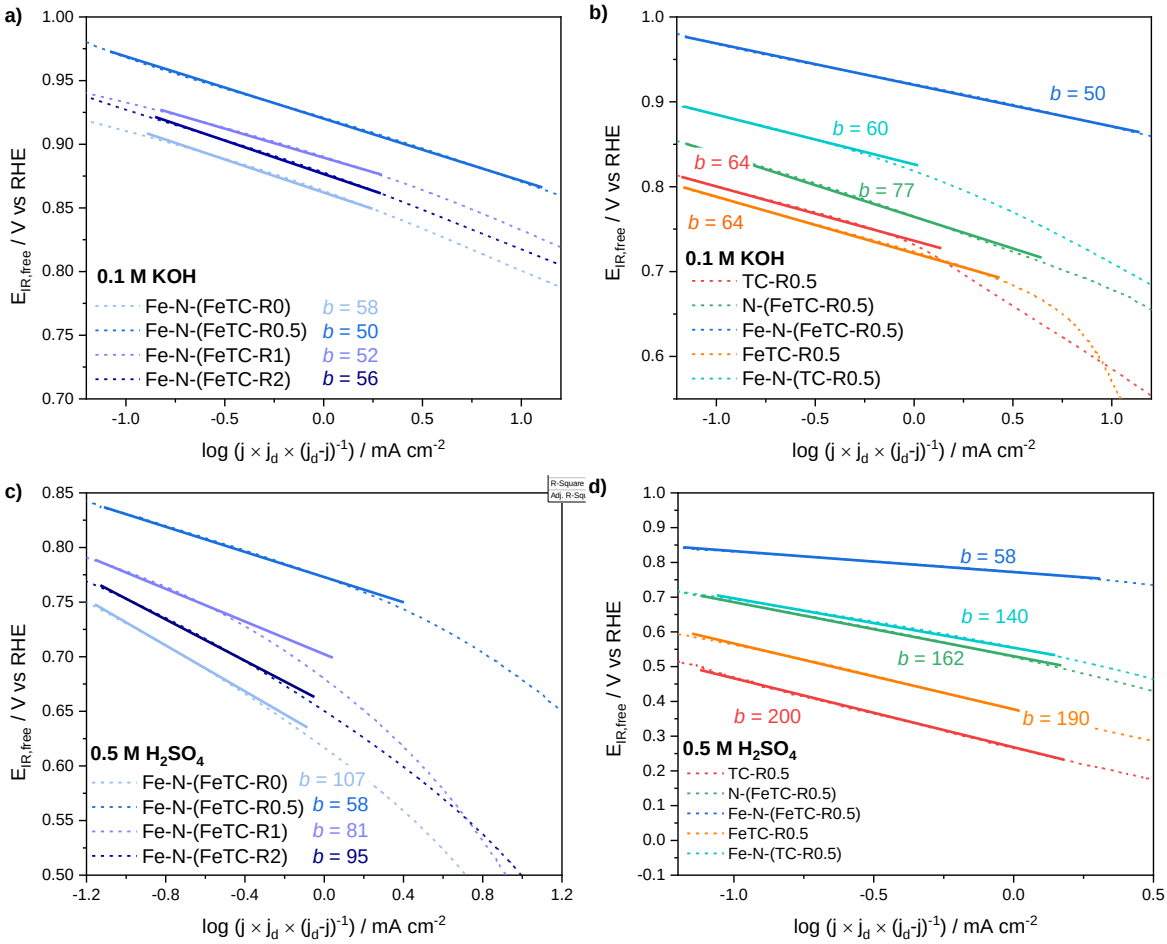

Figure S13. Tafel plots of tannin-derived electrocatalyst in 0.1 M KOH (a, b) and 0.5 M H_2SO_4 (c, d) aqueous solutions saturated with oxygen at 1600 rpm.

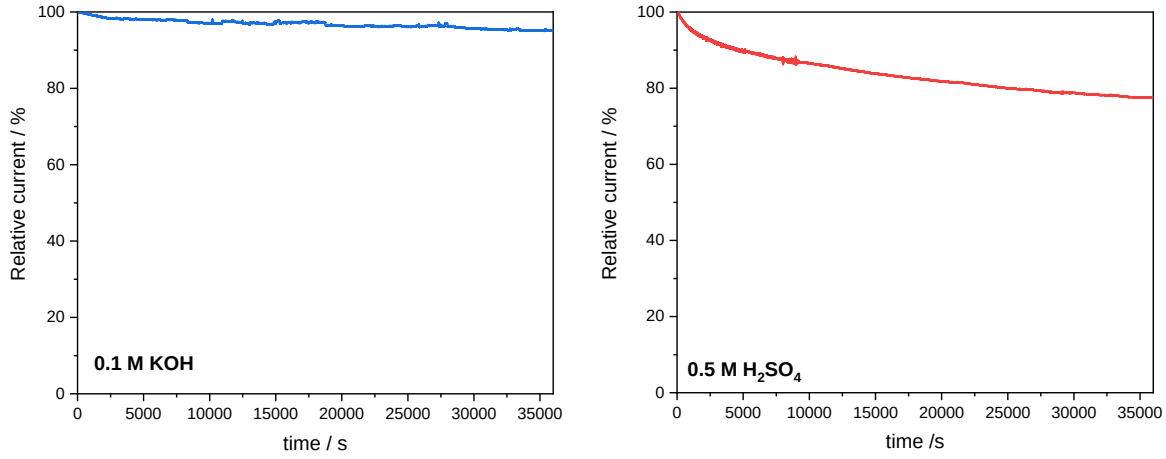

Figure S14. Chronoamperometric responses under continuous oxygen bubbling of Fe-N-(FeTC-R0.5) catalyst and Pt/C at 1600 rpm and at 0.7 V vs. RHE in 0.1 M KOH (left) and at 0.6 V vs. RHE in 0.5 M H_2SO_4 (right).

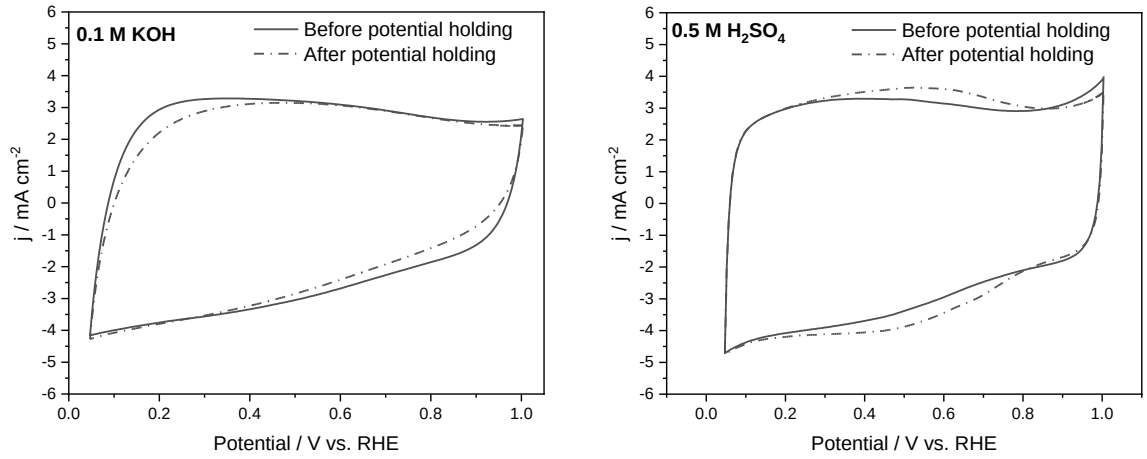

Figure S15. CV curves of Fe-N-(FeTC-R0.5) before (solid curves) and after (dotted curves) chronoamperometric experiments at 0.7 V vs. RHE in 0.1 M KOH (left) and at 0.6 V vs. RHE in 0.5 M H_2SO_4 (right) aqueous solutions saturated with oxygen at 20 mV s^{-1}.

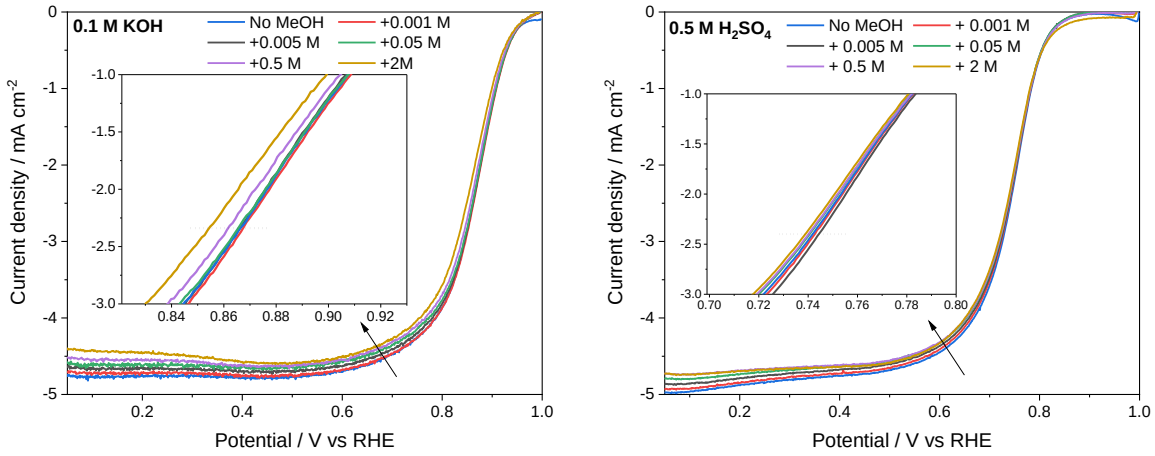

Figure S16. Methanol tolerance of Fe-N-(FeTC-R0.5) in O_2-saturated electrolytes: 0.1 M KOH (left) and 0.5 M H_2SO_4 (right). Insets show zoomed-in current density vs. potential in the mixed controlled region.

Table S1. Nomenclature of as-synthesized materials and experimental details in the hydrochar synthesis and carbonization stages.

Name	**Description**	**Hydrochar synthesis (stage 1)**		**Carbonization (stage 2)**		
		Pluronic-127/ tannin ratio	$FeCl_3$	Urea	$FeCl_3$	900 ºC
THC-R0.5	Tannin-derived hydrochar	0.5	-	-	-	-
FeTHC-R0	Tannin-Fe(III)-derived hydrochar in the absence of Pluronic-127	0.0	√	-	-	-
FeTHC-R0.5	Tannin-Fe(III)-derived hydrochar using R = 0.5	0.5	√	-	-	-
FeTHC-R1	Tannin-Fe(III)-derived hydrochar using R = 1	1	√	-	-	-
FeTHC-R2	Tannin-Fe(III)-derived hydrochar using R = 2	2	√	-	-	-
Fe-N-(FeTC-R0)	Fe_3C@Fe-N-C catalyst using FeTHC-R0 as the carbon precursor	0.0	√	√	√	√
Fe-N-(FeTC-R0.5)	Fe_3C@Fe-N-C catalyst using FeTHC-R0.5 as the carbon precursor	0.5	√	√	√	√
Fe-N-(FeTC-R1)	Fe_3C@Fe-N-C catalyst using FeTHC-R1 as the carbon precursor	1.0	√	√	√	√
Fe-N-(FeTC-R2)	Fe_3C@Fe-N-C catalyst using FeTHC-R2 as the carbon precursor	2.0	√	√	√	√
FeTC-R0.5	Partially graphitized carbon containing Fe from the direct carbonization of FeTHC	0.5	√	-	-	√
N-(FeTC-R0.5)	Fe_3C@Fe-N-C catalyst using FeTHC-R0.5 as the carbon precursor	0.5	√	√	-	√
Fe-(FeTC-R0.5)	Fe_3C@C catalyst using FeTHC-R0.5 as the carbon precursor	0.5	√	-	√	√
TC-R0.5	Amorphous carbon from direct carbonization of THC	0.5	-	-	-	√
Fe-N-(TC-R0.5)	Fe_3C@Fe-N-C catalyst using THC-R0.5 as the carbon precursor	0.5	-	√	√	√

Table S2. Chemical composition of tannin-derived electrocatalysts determined by elemental analysis and ICP-AES.

Material	**EA and ICP-AES / wt. %**			
	C	**H**	**N**	**Fe**
Fe-N-(FeTC-R0)	82.03	1.22	1.48	1.50
Fe-N-(FeTC-R0.5)	85.66	1.50	2.95	1.80
Fe-N-(FeTC-R1)	90.09	0.59	1.50	2.10
Fe-N-(FeTC-R2)	89.49	0.40	1.62	1.20
FeTC-R0.5	90.35	0.62	0.24	0.52
N-(FeTC-R0.5)	93.47	0.52	0.93	1.30
TC-R0.5	95.03	0.71	0.20	0.00
Fe-N-(TC-R0.5)	91.39	0.51	1.13	1.50

Table S3. Total Fe and N contents by XPS and distribution of nitrogen species (considering the total N content by XPS) in tannin-derived electrocatalysts, from deconvolution of the N1s XPS spectrum.

Catalyst	Fe-N-(FeTC-R0)	**Fe-N-(FeTC-R0.5)**	Fe-N-(FeTC-R1)	Fe-N-(FeTC-R2)	N-(FeTC-R0.5)	Fe-N-(TC-R0.5)
Fe / at.%	0.5	0.3	0.3	0.6	0.7	0.8
N / at.%	1.0	1.4	1.6	0.9	0.7	1.0
Pyridinic N / at.%	0.14	0.29	0.21	0.17	0.12	0.21
N-Fe / at.%	0.25	0.35	0.30	0.19	0.13	0.31
Pyrrolic N / at.%	0.38	0.55	0.72	0.33	0.32	0.35
Graphitic N / at.%	0.17	0.16	0.29	0.16	0.09	0.05
NO_x / at.%	0.06	0.04	0.07	0.06	0.04	0.10

Table S4. Results of fitting the Mössbauer spectrum of Fe-N-(FeTC-R0.5) with two sextet and two doublet components. The table reports values of isomer shift (IS), quadrupole splitting (QS), linewidth (LW) and hyperfine field (HF).

Component	IS / mm s^{-1}	QS / mm s^{-1}	LW / mm s^{-1}	HF / T	Assignment	Relative absorption area / %
Sextet 1	0.30	-	0.57	26	Fe_3C	76
Sextet 2	0.72	-	0.72	50	Fe_2O_3	10
D1	0.53	0.90	0.86	-	Fe(III)-N_x	6
D2	0.53	2.83	2.10	-	Fe(II)-N_x	8

Table S5. Main textural properties of tannin-derived electrocatalysts.

Material	A_{BET} /m^2 g^{-1}	S_{NLDFT} / m^2 g^{-1}	$S_{MES,NLDFT}$ / m^2 g^{-1}	$S_{\mu,NLDFT}$ / m^2 g^{-1}	V_{NLDFT} / cm^3 g^{-1}	$V_{MES,NLDFT}$ / cm^3 g^{-1}	$V_{\mu,NLDFT}$ / cm^3 g^{-1}	$w_{\mu,av\text{-}NLDFT}$ / nm	$w_{MES,av\text{-}NLDFT}$ / nm	$w_{av\text{-}NLDFT}$ / nm
Fe-N-(FeTC-R0)	321	340	58	282	0.40	0.28	0.12	0.97	17.58	13.23
Fe-N-(FeTC-R0.5)	760	849	71	778	0.65	0.36	0.29	0.87	16.19	9.43
Fe-N-(FeTC-R1)	446	519	55	465	0.42	0.25	0.16	0.84	15.34	9.59
Fe-N-(FeTC-R2)	670	780	59	720	0.52	0.27	0.25	0.83	15.07	8.21
FeTC-R0.5	539	882	91	790	0.44	0.22	0.22	0.68	8.17	4.41
N-(FeTC-R0.5)	421	630	85	544	0.39	0.23	0.16	0.73	9.08	5.73
TC-R0.5	612	1068	149	919	0.62	0.37	0.25	0.65	5.23	3.43
Fe-N-(TC-R0.5)	289	355	76	279	0.49	0.39	0.09	0.78	17.36	14.34

A_{BET}: BET area from the N_2 adsorption isotherms. S_{NLDFT} and $S_{\mu,NLDFT}$: specific surface area and micropore surface area, respectively, by the 2D-NLDFT-HS model from N_2 and CO_2 adsorption isotherms. $S_{MES,NLDFT}$: mesopore volume ($S_{MES,NLDFT} = S_{NLDFT} - S_{\mu,NLDFT}$). V_{NLDFT} and $V_{\mu,NLDFT}$: total pore volume and micropore volume, respectively, by application of the 2D-NLDFT-HS model to N_2 and CO_2 adsorption isotherms. $V_{MES,NLDFT}$: mesopore volume ($V_{MES,NLDFT} = V_{NLDFT} - V_{\mu,NLDFT}$). $w_{av\text{-}NLDFT}$, $w_{MES,av\text{-}NLDFT}$ and $w_{\mu,av\text{-}NLDFT}$: average widths of pores mesopores and micropores, respectively, by application of the 2D-NLDFT-HS model to N_2 and CO_2 adsorption isotherms.

Table S6. ORR parameters of tannin-derived electrocatalysts and Pt/C catalysts in alkaline (0.1 M KOH) and acidic (0.5 M H_2SO_4) media.

Catalyst	Alkaline					Acidic				
	Onset potential /V @ 0.1 mA cm^{-2}	**$E_{1/2}$ /V**	**J_L /mA cm^{-2}**	**H_2O_2 /% @ 0.7 V**	**n @ 0.7 V**	**Onset potential /V @ 0.1 mA cm^{-2}**	**$E_{1/2}$ / V**	**J_L /mA cm^{-2}**	**H_2O_2 /% @ 0.5 V**	**n @ 0.5 V**
Fe-N-(FeTC-R0)	0.91	0.80	-4.99	2.7	3.95	0.73	0.51	-4.58	40.1	3.20
Fe-N-(FeTC-R0.5)	0.97	0.87	-4.88	1.5	3.97	0.85	0.74	-4.97	9.6	3.80
Fe-N-(FeTC-R1)	0.93	0.84	-4.34	1.9	3.96	0.78	0.56	-4.56	31.2	3.38
Fe-N-(FeTC-R2)	0.92	0.82	-4.53	1.8	3.96	0.75	0.56	-4.64	31.3	3.37
FeTC-R0.5	0.79	0.68	-3.33	33.1	3.33	0.56	0.28	-2.98	49.9*	3.01*
N-(FeTC-R0.5)	0.84	0.72	-2.77	24.5	3.51	0.68	0.41	-3.87	11.3	3.77
TC-R0.5	0.80	0.65	-3.20	44.2	3.12	0.46	-	-	51.9*	2.96*
Fe-N-(TC-R0.5)	0.88	0.75	-3.51	6.6	3.87	0.69	0.43	-4.33	40.2	3.20
Pt/C	0.96	0.83	-5.37	2.7	3.95	0.92	0.82	-4.97	0.4	3.99

* H_2O_2 or n @0.7 V

Table S7. Summary of activity ($E_{1/2}$) and stability (in terms of current retention after chronoamperometry (CA) tests) in 0.1 M KOH and 0.5 M H_2SO_4 of the Fe-N-(FeTC-R0.5) material presented here, and compared with biomass-derived M-N-C catalysts from the literature.

Catalyst	Carbon precursor	0.1 M KOH		0.5 M H_2SO_4[a]		Experimental conditions for CA		Ref.
		$E_{1/2}$ / V vs. RHE	Current retention / %	$E_{1/2}$ / V vs. RHE	Current retention / %	Time / s	E / V	
Fe-N-(FeTC-R0.5)	Mimosa tannin	0.87	98 95	0.74	89 79	10000 36000	0.7 V vs. RHE in 0.1 M KOH 0.6 V vs. RHE in 0.5 M H_2SO_4	This work
Fe–N/C_B-RGO (1)	Soybean dregs	0.83[c]	79	-	-	3600	-0.3 V vs. SCE	[1]
BP-K-A	Banana peels	0.84	95	0.57[b]	91[b]	10000	0.3 V vs. SCE in 0.1 M $HClO_4$	[2]
NCS-800	Typha orientalis	0.80	77	0.50[c]	80[c]	10000	0.1 V vs RHE	[3]
SC-FeCo–N@N-carbon	Sugarcane	0.81	78	-	-	10000	0.7 V vs. RHE	[4]
Fe-N-C_{wood}	Wood	-	-	0.70[b]	85[b,c]	10000	-	[5]
Fe/ChoCl/RGO	Sengon wood	0.84	90	-	-	16000	-	[6]
Fe-Pani-RGO 2 py	Sengon wood	-	-	0.74[b]	92[b]	16000	0.53 V vs. RHE in 0.1 M $HClO_4$	[7]
Fe/N/CNT@PCF	Willow catkins	0.72	89	-	-	20000	-0.4 V vs. Ag/AgCl	[8]
BY-Fe-A	Brewer's yeast	0.86	96	-	-	20000	0.68 V vs. RHE	[9]
RN350-Z(1-2)-1000	Legume root	0.87	92	0.72[b]	68[b]	30000	0.7 V vs. RHE in 0.1 M KOH 0.6 V vs. RHE in 0.1 M $HClO_4$	[10]
HDPC-800	Tea leaves	0.79	93	-	-	36000	-	[11]
M^+S^+C900-900	Spinach leaves	0.88	83	0.75	-	36000	0.88 V vs. RHE	[12]
FeCoNCR-a	Rapeseed cake	0.81	90	-	-	36000	0.5 V vs. RHE	[13]

[a] The electrolyte is 0.5 M H_2SO_4 unless otherwise specified. [b] The electrolyte is 0.1 M $HClO_4$. [c] Estimated from figures

Table S8. Comparison of Fe-N-(FeTC-R0.5) and other biomass-derived M-N-C catalysts in AEMFCs and PEMFCs.

Cathode catalyst	Carbon precursor	$E_{1/2}$ / V vs RHE from RDE[a]	Cathode Loading / mg cm^{-2}	Anode catalyst	Membrane	Membrane thickness / μm	Temp. / ºC	j[c] / mA cm^{-2}	PPD / mW cm^{-2}	Ref.
AEMFCS										
Fe-N-(FeTC-R0.5)	Tannin	0.87	1	PtRu/C	Modified FAA-3 / Fumatech	10	60	330	242	This work
PDCC_$ZnCl_2$	Peat	0.83	4	PtRu/C	FAA-3 / Fumatech	50	60	40[d]	51	[14]
Fe-LC-900	Waste leather	0.82	2	Pt/C	FAA / Fumatech	-	-	50[d]	50	[15]
Fe/N-F/CC-C	Corncob waste	0.92	0.5	Pt/C	Fumatech	50	45	25[d]	38	[16]
NBSCP	Bean sprouts	0.84	3	Pt/C	FAA-3 / Fumatech	50	60	200[d]	172	[17]
Fe-N-C-sucrose	Sucrose	0.81	4	Pt/C	AHA-neosepta	50	RT[b]	175[d]	118	[18]
L_FeMn	Lignin	0.87	0.8	PtRu/C	In-house	10	60	350[d]	261	[19]
FeCoNCR-a	Rapeseed cake	0.81	2	Pt/Ru/C	AF2-HLE8-10-X / Aemion	10	60	200[d]	131	[13]
Zn/Fe_{SA}-PC/950/NH_3	Waste pig blood	0.88	1	PtRu/C	FAA-3 / Fumatech	20	60	300[d]	230[d]	[20]
Fe-N-PDC-HA	Peat	0.87	1.1	PtRu/C	Xion Pention	20	80	1500[d]	1060	[21]
PEMFCS										
Fe-N-(FeTC-R0.5)	Tannin	0.74	4.1	Pt/C	Nafion NRE-211	25	80	414	200	This work
Co-N/C-3($ZnCl_2$)	Peat	-	4	Pt/C	Nafion HP	20	80	350[d]	210	[22]
CHbMg3s400900	Hemoglobine	-	5	Pt/C	Nafion N-112	50	80	250[d]	125	[23]
L_FeMn	Lignin	0.77	4.4	Pt/C	Nafion NR-211	25	80	150[d]	72	[19]

[a] RDE tests in 0.1 M KOH or 0.5 M H_2SO_4. [b] RT = room temperature. [c] j at 0.6 V for AEMFC and 0.4 V for PEMFC. [d] Estimated from figures

References

[1] Z. Yao, J. Ma, T.K.A. Hoang, M. Shi, A. Sun, High performance biomass-derived catalysts for the oxygen reduction reaction with excellent methanol tolerance, International Journal of Hydrogen Energy 45 (2020) 27026–27035. https://doi.org/10.1016/j.ijhydene.2020.07.023.

[2] J. Zhang, C. Zhang, Y. Zhao, I.S. Amiinu, H. Zhou, X. Liu, Y. Tang, S. Mu, Three dimensional few-layer porous carbon nanosheets towards oxygen reduction, Applied Catalysis B: Environmental 211 (2017) 148–156. https://doi.org/10.1016/j.apcatb.2017.04.038.

[3] P. Chen, L.-K. Wang, G. Wang, M.-R. Gao, J. Ge, W.-J. Yuan, Y.-H. Shen, A.-J. Xie, S.-H. Yu, Nitrogen-doped nanoporous carbon nanosheets derived from plant biomass: an efficient catalyst for oxygen reduction reaction, Energy Environ. Sci. 7 (2014) 4095–4103. https://doi.org/10.1039/C4EE02531H.

[4] H.-C. Kuo, S.-H. Liu, Y.-G. Lin, C.-L. Chiang, D.C.W. Tsang, Synthesis of FeCo–N@N-doped carbon oxygen reduction catalysts via microwave-assisted ammoxidation, Catal. Sci. Technol. 10 (2020) 3949–3958. https://doi.org/10.1039/D0CY00376J.

[5] D. Li, Z. Han, K. Leng, S. Ma, Y. Wang, J. Bai, Biomass wood-derived efficient Fe–N–C catalysts for oxygen reduction reaction, J Mater Sci 56 (2021) 12764–12774. https://doi.org/10.1007/s10853-021-06122-7.

[6] W. Sudarsono, W.Y. Wong, K.S. Loh, E.H. Majlan, N. Syarif, K.-Y. Kok, R.M. Yunus, K.L. Lim, Noble-free oxygen reduction reaction catalyst supported on Sengon wood (Paraserianthes falcataria L.) derived reduced graphene oxide for fuel cell application, International Journal of Energy Research 44 (2020) 1761–1774. https://doi.org/10.1002/er.5015.

[7] W. Sudarsono, W.Y. Wong, K.S. Loh, E.H. Majlan, N. Syarif, K.-Y. Kok, R.M. Yunus, K.L. Lim, I. Hamada, Sengon wood-derived RGO supported Fe-based electrocatalyst with stabilized graphitic N-bond for oxygen reduction reaction in acidic medium, International Journal of Hydrogen Energy 45 (2020) 23237–23253. https://doi.org/10.1016/j.ijhydene.2020.05.158.

[8] M. Li, Y. Xiong, X. Liu, C. Han, Y. Zhang, X. Bo, L. Guo, Iron and nitrogen co-doped carbon nanotube@hollow carbon fibers derived from plant biomass as efficient catalysts for the oxygen reduction reaction, J. Mater. Chem. A 3 (2015) 9658–9667. https://doi.org/10.1039/C5TA00958H.

[9] G. Wang, H. Peng, X. Qiao, L. Du, X. Li, T. Shu, S. Liao, Biomass-derived porous heteroatom-doped carbon spheres as a high-performance catalyst for the oxygen reduction reaction, International Journal of Hydrogen Energy 41 (2016) 14101–14110. https://doi.org/10.1016/j.ijhydene.2016.06.023.

[10] M. Hao, R. Dun, Y. Su, L. He, F. Ning, X. Zhou, W. Li, In situ self-doped biomass-derived porous carbon as an excellent oxygen reduction electrocatalyst for fuel cells and metal–air batteries, J. Mater. Chem. A 9 (2021) 14331–14343. https://doi.org/10.1039/D1TA01417J.

[11] Z. Guo, Z. Xiao, G. Ren, G. Xiao, Y. Zhu, L. Dai, L. Jiang, Natural tea-leaf-derived, ternary-doped 3D porous carbon as a high-performance electrocatalyst for the oxygen reduction reaction, Nano Res. 9 (2016) 1244–1255. https://doi.org/10.1007/s12274-016-1020-2.

[12] X. Liu, C. Culhane, W. Li, S. Zou, Spinach-Derived Porous Carbon Nanosheets as High-Performance Catalysts for Oxygen Reduction Reaction, ACS Omega 5 (2020) 24367–24378. https://doi.org/10.1021/acsomega.0c02673.

[13] S. Juvanen, A. Sarapuu, M. Mooste, M. Käärik, U. Mäeorg, A. Kikas, V. Kisand, J. Kozlova, A. Treshchalov, J. Aruväli, J. Leis, A. Tamm, K. Tammeveski, Electroreduction of oxygen on iron- and cobalt-containing nitrogen-doped carbon catalysts prepared from the rapeseed press cake, Journal of Electroanalytical Chemistry 920 (2022) 116599. https://doi.org/10.1016/j.jelechem.2022.116599.

[14] P. Teppor, R. Jäger, M. Paalo, A. Adamson, M. Härmas, O. Volobujeva, J. Aruväli, R. Palm, E. Lust, Peat as a carbon source for non-platinum group metal oxygen electrocatalysts and AEMFC cathodes, International Journal of Hydrogen Energy 47 (2022) 16908–16920. https://doi.org/10.1016/j.ijhydene.2022.03.199.

[15] R. Soni, S.N. Bhange, S. Kurungot, A 3-D nanoribbon-like Pt-free oxygen reduction reaction electrocatalyst derived from waste leather for anion exchange membrane fuel cells and zinc-air batteries, Nanoscale 11 (2019) 7893–7902. https://doi.org/10.1039/C9NR00977A.

[16] S.K. Das, A. Kesh, S. Akula, A.K. Sahu, N-, F-, and Fe-Doped Mesoporous Carbon Derived from Corncob Waste and Creating Oxygen Reduction Reaction Active Centers with a Maximum Charge Density of ≥0.25 for a Polymer Electrolyte Fuel Cell Catalyst, Energy Fuels 36 (2022) 2108–2122. https://doi.org/10.1021/acs.energyfuels.1c03174.
[17] D.W. Lee, J.-H. Jang, I. Jang, Y.S. Kang, S. Jang, K.Y. Lee, J.H. Jang, H.-J. Kim, S.J. Yoo, Bio-Derived Co2P Nanoparticles Supported on Nitrogen-Doped Carbon as Promising Oxygen Reduction Reaction Electrocatalyst for Anion Exchange Membrane Fuel Cells, Small 15 (2019) 1902090. https://doi.org/10.1002/smll.201902090.
[18] I.J.R. Sarkar, S.G. Peera, R. Chetty, Fe–N–C catalyst derived from solid-state coordination complex as durable oxygen reduction electrocatalyst in alkaline electrolyte, Ionics 26 (2020) 5685–5696. https://doi.org/10.1007/s11581-020-03722-2.
[19] M. Muhyuddin, A. Friedman, F. Poli, E. Petri, H. Honig, F. Basile, A. Fasolini, R. Lorenzi, E. Berretti, M. Bellini, A. Lavacchi, L. Elbaz, C. Santoro, F. Soavi, Lignin-derived bimetallic platinum group metal-free oxygen reduction reaction electrocatalysts for acid and alkaline fuel cells, Journal of Power Sources 556 (2023) 232416. https://doi.org/10.1016/j.jpowsour.2022.232416.
[20] H.S. Kim, J. Lee, J.-H. Jang, H. Jin, V.K. Paidi, S.-H. Lee, K.-S. Lee, P. Kim, S.J. Yoo, Waste pig blood-derived 2D Fe single-atom porous carbon as an efficient electrocatalyst for zinc–air batteries and AEMFCs, Applied Surface Science 563 (2021) 150208. https://doi.org/10.1016/j.apsusc.2021.150208.
[21] P. Teppor, R. Jäger, M. Koppel, O. Volobujeva, R. Palm, M. Månsson, E. Härk, Z. Kochovski, J. Aruväli, K. Kooser, S. Granroth, T. Käämbre, J. Nerut, E. Lust, Unlocking the porosity of Fe–N–C catalysts using hydroxyapatite as a hard template en route to eco-friendly high-performance AEMFCs, Journal of Power Sources 591 (2024) 233816. https://doi.org/10.1016/j.jpowsour.2023.233816.
[22] R. Jäger, P. Teppor, M. Paalo, M. Härmas, A. Adamson, O. Volobujeva, E. Härk, Z. Kochovski, T. Romann, R. Härmas, J. Aruväli, A. Kikas, E. Lust, Synthesis and Characterization of Cobalt and Nitrogen Co-Doped Peat-Derived Carbon Catalysts for Oxygen Reduction in Acidic Media, Catalysts 11 (2021) 715. https://doi.org/10.3390/catal11060715.
[23] J. Maruyama, T. Hasegawa, T. Amano, Y. Muramatsu, E.M. Gullikson, Y. Orikasa, Y. Uchimoto, Pore Development in Carbonized Hemoglobin by Concurrently Generated MgO Template for Activity Enhancement as Fuel Cell Cathode Catalyst, ACS Appl. Mater. Interfaces 3 (2011) 4837–4843. https://doi.org/10.1021/am2013294.